entropy

MDPI

Article

Effects of Composition Adjustment on Soft Magnetic Properties and Microstructure in Fe-Co-Ni Medium-Entropy Alloys

Pin Jiang [1], Zitong He [1], Nan Lu [1], Shuyan Zhang [2], Xiaohua Tan [1] and Hui Xu [1,*]

[1] State Key Laboratory of Materials for Advanced Nuclear Energy, Shanghai University, Shanghai 200444, China; 17855547568@163.com (P.J.)
[2] Suzhou Wave Vector Advanced Materials Technology Co., Ltd., Suzhou 215331, China
* Correspondence: huixu8888@shu.edu.cn; Tel.: +86-21-5633-7887

Abstract

Fe-Co-Ni medium-entropy alloys (MEAs) show great soft-magnetic potential, yet the effect of intrinsic Fe-Co-Ni ratio adjustment (without extra alloying additions) on microstructure and magnetic behaviors is poorly clarified. In this study, $Fe_{100-x}(Co_{0.5}Ni_{0.5})_x$ (x = 10–80 at%) alloys were prepared by vacuum arc melting and characterized by X-ray diffraction (XRD), scanning electron microscopy-energy dispersive X-ray spectroscopy (SEM-EDS), electron backscatter diffraction (EBSD), vibrating sample magnetometer (VSM) and direct current (DC) soft magnetic measurements to reveal the influences of composition tuning on phase, microstructure, mechanical and soft-magnetic properties. With increasing x, the alloys transform from single BCC, through BCC+FCC dual-phase, to single FCC structure. Notably, all alloys with $x \leq 40$ possess high saturation magnetization (M_s) exceeding 200 Am²/kg. This high M_s is attributed to a Fe-Co-enriched BCC phase. Across the whole composition range, M_s monotonically decreases from 220 Am²/kg to 138 Am²/kg, while coercivity (H_c) varies non-monotonically and peaks at x = 40. The maximum H_c originates from Ni grain-boundary segregation, fine grains, high fraction of low-angle grain boundaries (LAGBs) and severe local strain concentration. The x = 70 single FCC alloy delivers optimal DC soft-magnetic properties: initial permeability (μ_i) of 539, maximum permeability (μ_m) of 1464, low H_c of 36 A/m and saturation flux density (B_m) of 1.60 T. This work clarifies how phase constitution, grain features and strain govern magnetic responses and provides practical guidelines for designing high performance soft-magnetic MEAs.

Keywords: medium-entropy alloys; soft magnetic properties; composition adjustment; microstructure

Academic Editor: Jürn W.P. Schmelzer

Received: 24 October 2026
Revised: 16 November 2026
Accepted: 24 November 2026
Published: 26 November 2026

Copyright: © 2026 by the authors. Licensee MDPI, Basel, Switzerland. This article is an open access article distributed under the terms and conditions of the Creative Commons Attribution (CC BY) license.

1. Introduction

Soft magnetic materials (SMMs) are indispensable functional materials in modern electrical and electronic systems, serving as core components in power generation and conversion, rotating electrical machines, transformers, and electromagnetic devices [1–3]. With the rapid development of electric vehicles, high-speed railways, and more electric aircraft, there is an urgent demand for soft magnetic materials that simultaneously possess high saturation magnetization (M_s) and low coercivity (H_c) [4–6]. However, conventional SMMs face persistent trade-off among these properties. For example, permalloy features high permeability (μ), but its M_s trend to be low [7,8]. Soft ferrites exhibit superior

electrical resistivity, yet have low M_s [9,10]. Silicon steel delivers high M_s, though its eddy current loss remains high [11].

High-entropy alloys (HEAs), defined as multi-principal-component alloys with five or more elements, have attracted extensive research interest owing to their unique core effects, including high-entropy, lattice distortion, sluggish diffusion, and cocktail effect [12–16]. These distinctive features endow HEAs with superior magnetic performance. On this basis, medium-entropy alloys (MEAs) with three or four elements further expand the family of multi-principal alloys, offering greater flexibility in property optimization [17,18]. Among them, equiatomic FeCoNi MEA stands out as a promising soft magnetic candidate. It exhibits favorable soft magnetic performance (SMPs), combining high M_s and relatively low H_c, alongside good ductility and mechanical robustness [19,20]. Such integrated magnetic-mechanical advantages make FeCoNi MEA a competitive alternative to traditional soft magnetic materials.

Although equiatomic FeCoNi MEA exhibits great SMPs, researchers continue to explore ways to enhance it. Most existing attempts to tailor the SMPs of FeCoNi MEAs rely on alloying with extrinsic elements. Such as, Radhakrishnan et al. [21] demonstrated that Cr doping into FeCoNi can effectively reduce H_c. Yang et al. [22] investigated FeCoNi(AlSi)$_x$ alloys, found that the introduction of Al and Si refined domain structures and lowered H_c. Liu et al. [23] designed FeCoNiSi$_x$Al$_{0.4}$ HEAs, and found that rising Si content suppressed M_s. Peng et al. [24] demonstrated that the addition of Al can improve the alternating current soft magnetic properties (AC SMPs) of FeCoNi MEA. However, relatively few studies have systematically explored how adjusting the intrinsic atomic ratio among Fe, Co and Ni modulates the magnetic behaviors and microstructure without introducing extra elements. For example, Tan et al. [25] constructed a series of Fe-Co-Ni ternary MEAs and revealed the variation trends of magnetic properties with elemental ratios, but the mechanism of how composition driven microstructure evolution governs magnetic properties is not in-depth in their report. Distinct from many previous studies relying on extrinsic element doping, this work modulates only the intrinsic Fe-Co-Ni atomic proportion. We systematically decouple the combined influences of phase constitution, Ni grain-boundary segregation, grain size, low-angle grain boundary fraction, and local strain concentration on both saturation magnetization and coercivity (H_c), which provides clear microstructure-magnetic property links for ternary Fe-Co-Ni MEAs.

In this work, we systematically investigate the SMPs and microstructure of $Fe_{100-x}(Co_{0.5}Ni_{0.5})_x$ (x = 10–80 at%) alloys. Combined with X-ray diffraction (XRD), scanning electron microscopy-energy dispersive X-ray spectroscopy (SEM-EDS) and electron backscatter diffraction (EBSD), we clarify the mechanism of phase constitution, grain size, low-angle grain boundaries (LAGBs), and strain concentration affect M_s and H_c. The findings of this work provides not only a fundamental understanding of the relationships between microstructure and magnetic properties in FeCoNi MEAs, but also provides practical composition guidelines for designing high-performance soft magnetic MEAs, thereby laying a foundation for the application of advanced electromagnetic devices.

2. Materials and Methods

The $Fe_{100-x}(Co_{0.5}Ni_{0.5})_x$ (x = 10–80 at%) alloys were fabricated by vacuum arc melting under an argon atmosphere using high-purity (≥99.99 wt%) Fe, Co, and Ni elements. To ensure chemical homogeneity, each ingot was remelted four times. Subsequently, the homogenized ingots were suction-cast into a water-cooled copper mold to produce plate-shaped samples with dimensions of 100 mm × 10 mm × 2 mm for subsequent characterization. The saturation magnetization (M_s) and coercivity (H_c) of the alloys were measured using a vibrating sample magnetometer (VSM, Lakeshore 7407, Westerville, OH, USA) under an applied magnetic field of 1.8 T. The direct current (DC) soft magnetic properties

of the samples were evaluated at room temperature using a soft magnetic measurement system (FE-2100SD, Forever elegance, Loudi, China) equipped with a permeameter under an applied field of 5000 A/m. The Vickers hardness measurements were conducted using a Vickers hardness tester (HXD-1000TMC/LCD, Sunny Hengping Scientiffc Instrument, Shanghai, China) with a load of 0.98 N and a dwell time of 10 s. For each sample, nine indentations were performed at different locations to ensure measurement reliability, and the average value was taken as the final hardness result. The crystal structures of the alloys were identified by X-ray diffraction (XRD, Empyrean, PANalytical Corporation, Almelo, Holland) using Cu Kα radiation. The diffraction patterns were collected over a scanning range of 20–100° at a step size of 0.02°. The surface morphology and elemental distributions of the alloys were characterized using scanning electron microscopy (SEM, Bruker e-FlashFS, Bruker Nano GmbH, Hamburg, Germany) equipped with an energy-dispersive X-ray spectroscopy (EDS) system. The microstructural characteristics, including phase distribution, grain size, grain boundary distribution characteristics and strain concentration were further investigated by electron backscatter diffraction (EBSD, Bruker e-FlashFS, Bruker Nano GmbH, Hamburg, Germany). The SEM and EBSD measurements were performed at an accelerating voltage of 15 kV and 20 kV, respectively.

3. Results

3.1. Magnetic Properties

Figure 1a presents the hysteresis loops of the $Fe_{100-x}(Co_{0.5}Ni_{0.5})_x$ (x = 10–80 at%) alloys measured by VSM. All alloys exhibit typical soft magnetic characteristics. Figure 1b illustrates that the M_s of $Fe_{100-x}(Co_{0.5}Ni_{0.5})_x$ (x = 10–80 at%) alloys continuously decreases from 220 Am²/kg to 138 Am²/kg with increasing x, while maintaining an ultrahigh level of above 200 Am²/kg when $x \leq 40$. It is worth noting that M_s decreases significantly when x = 50. However, the H_c increases first and then decreases. It rises rapidly to 2249 A/m at x = 40, followed by a sharp drop at x = 50, and then reaches a minimum value of 224 A/m at x = 70. The corresponding M_s and H_c values are summarized in Table 1.

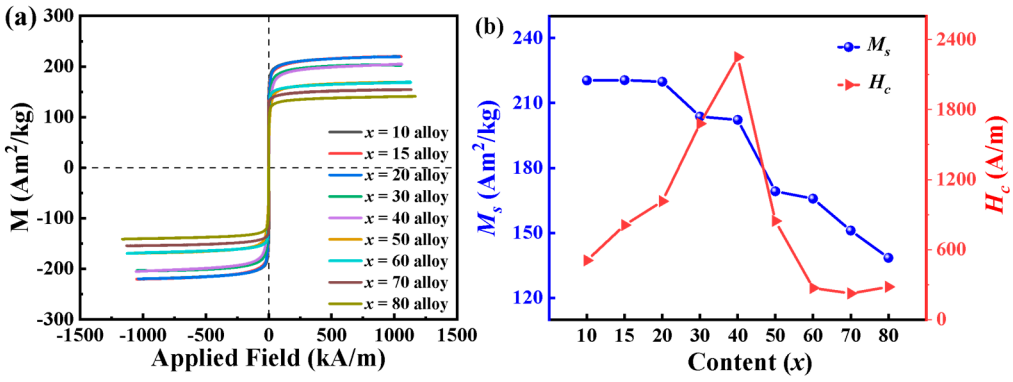


Figure 1. (**a**) The hysteresis loops of $Fe_{100-x}(Co_{0.5}Ni_{0.5})_x$ (x = 10–80 at%) alloys with an applied magnetic field of 1.8 T, (**b**) line plots of M_s and H_c as a function of Co and Ni contents.

Figure 2 compares the M_s and H_c of $Fe_{100-x}(Co_{0.5}Ni_{0.5})_x$ (x = 10–80 at%) alloys in this work with those previously reported medium/high-entropy alloys (M/HEAs). The comparison reveals that the present alloys are located in the upper-left region of the map, demonstrating a favorable combination of high M_s and low H_c values. In addition, several alloys exhibit M_s values, significantly higher than other reported M/HEAs.

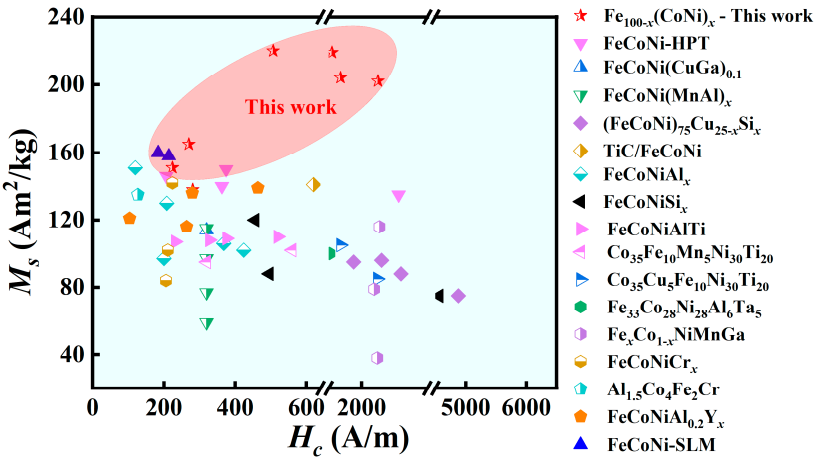


Figure 2. Comparison of M_s and H_c of $Fe_{100-x}(Co_{0.5}Ni_{0.5})_x$ (x = 10–80 at%) alloys with other reported magnetic M/HEAs [20,26–39].

Table 1. The magnetic parameters of $Fe_{100-x}(Co_{0.5}Ni_{0.5})_x$ (x = 10–80 at%) alloys.

x	VSM (H_m = 1.8 T)		DC (H_m = 5 kA/m)					
	M_s (Am^2/kg)	H_c (A/m)	μ_i	μ_m	B_m (T)	H_c (A/m)	B_r (mT)	P_u (J/m^3)
10	220	507	130	610	1.72	289	411	1752
15	220	810	80	417	1.55	502	473	2431
20	219	1014	117	363	1.42	685	551	2902
30	204	1680	93	262	1.25	1184	636	4383
40	202	2249	82	204	1.07	1445	590	4596
50	169	845	163	441	1.13	281	253	945
60	165	270	472	1393	1.60	53	126	221
70	151	224	539	1464	1.60	36	81	215
80	138	281	308	1284	1.36	56	124	249

Figure 3 presents the line chart of the DC soft magnetic parameters of the $Fe_{100-x}(Co_{0.5}Ni_{0.5})_x$ (x = 10–80 at%) alloys. With increasing x, the μ_i, μ_m, and B_m values exhibit a decreasing followed by an increasing trend, whereas the H_c, B_r, and P_u values show an opposite variation tendency. At x = 70, the alloy achieves the highest μ_i, μ_m, and B_m values of 539, 1464, and 1.60 T, respectively, together with the lowest H_c, B_r, and P_u values of 36 A/m, 81 mT, and 215 J/m^3, respectively, indicating the optimal DC soft magnetic performance. In contrast, the x = 40 alloy exhibits the lowest μ_i, μ_m, and B_m values of 82, 204, and 1.07 T, respectively, and the highest H_c, B_r, and P_u values of 1445 A/m, 590 mT, and 4596 J/m^3, respectively, which are significantly higher than the alloys with other compositions. The specific values are listed in Table 1. Figure 4 summarizes the B_m and H_c values of selected reported magnetic H/MEAs and the $Fe_{100-x}(Co_{0.5}Ni_{0.5})_x$ (x = 10–80 at%) alloys. The results demonstrate that the x = 60 and 70 alloys possess relatively high B_m values while maintaining low H_c values, showing superior soft magnetic properties compared with most previously reported alloys.

Notably, the H_c measured by VSM differs from the DC soft magnetic measuring instrument, the H_c measured by VSM is larger. We consider this discrepancy may arise from the following two aspects: (1) VSM performs open-circuit measurements, whereas the DC soft magnetic measuring instrument performs closed-circuit measurements. (2) The magnetic field applied during VSM testing is 18000 Oe, whereas that applied by the DC soft magnetic measuring instrument is only 5000 A/m (~62.5 Oe).

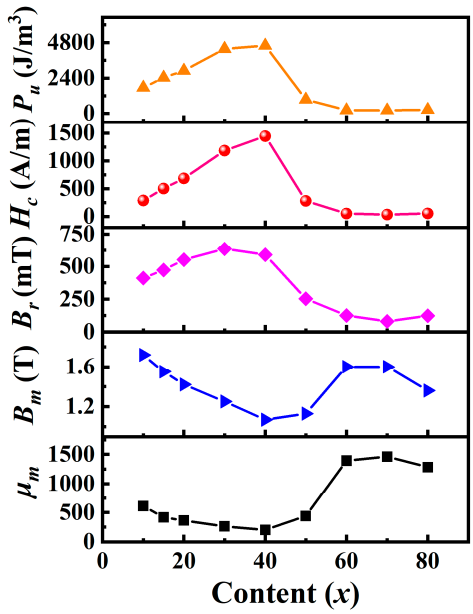


Figure 3. DC soft magnetic parameters of $Fe_{100-x}(Co_{0.5}Ni_{0.5})_x$ (x = 10–80 at%) alloys.

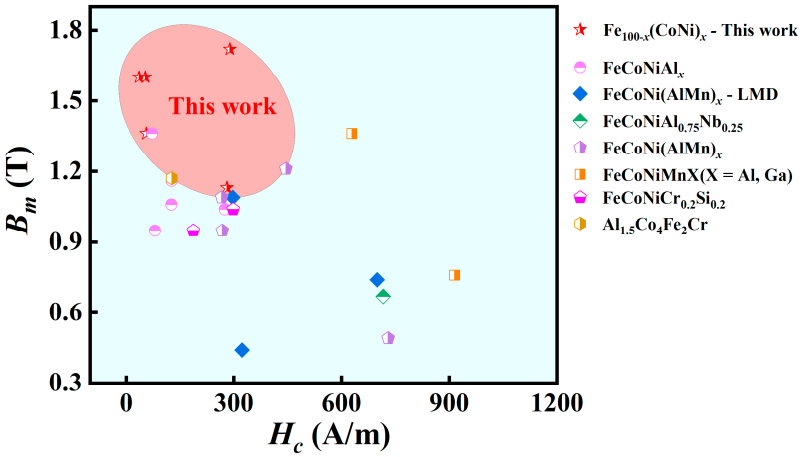


Figure 4. Comparison of the B_m and H_c between the $Fe_{100-x}(Co_{0.5}Ni_{0.5})_x$ (x = 10–80 at%) alloys and other reported magnetic M/HEAs [40–44].

3.2. Mechanical Properties

Figure 5 presents the Vickers hardness of the $Fe_{100-x}(Co_{0.5}Ni_{0.5})_x$ (x = 10–80 at%) alloys. With the increase of x, the Vickers hardness of the alloy first rises with a consistent increment and reaches the highest hardness of 287 HV at x = 40. We attribute this results to the increased Co content, since Co possesses relatively high hardness, and the alloy is expected to be the single BCC phase [45]. Afterwards, the hardness drops abruptly to 183 HV at x = 50, which we ascribe to the emergence of the FCC phase in the alloy. When $x \geq 60$, the hardness decreases further, and the alloy may exist a single FCC phase. The specific values are summarized in Table S1 of the Supplementary Materials.

We suggest that this may be related to several factors as follows: (1) Owing to the differences in crystal structure and slip systems, the FCC structure is softer, whereas the BCC structure is intrinsically harder. Accordingly, the hardness of the alloys with $x \leq 40$ is markedly higher than that of the alloys with $x \geq 60$ [46]. (2) For $x \leq 40$, the smaller Co/Ni atoms substitute for the larger Fe atoms, the resulting severe local elastic strain field effectively pins dislocations and enhances the solid-solution strengthening effect, which is an important driving force for the continuous increase in hardness [47]. (3) For $x \leq 40$, the

alloys exhibit a fine grain size and hence a larger number of grain boundaries, which exert strong pinning on dislocations. Moreover, Ni segregation at the grain boundaries further reinforces this grain-boundary pinning effect, leading to a relatively high hardness [48].

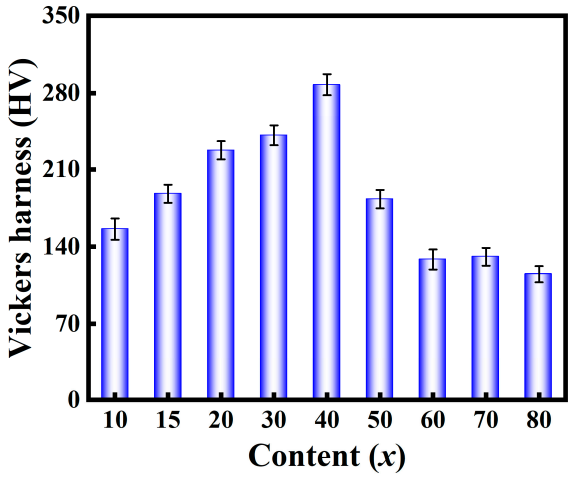


Figure 5. The Vickers hardness of $Fe_{100-x}(Co_{0.5}Ni_{0.5})_x$ (x = 10–80 at%) alloys.

3.3. X-Ray Diffraction

The XRD patterns of the $Fe_{100-x}(Co_{0.5}Ni_{0.5})_x$ (x = 10–80 at%) alloys are presented in Figure 6. As shown in Figure 6a, the contents of Fe, Co and Ni significantly influence the crystal structures of the alloys. With increasing x, the alloys undergo a phase transition from a single BCC phase ($x \leq 40$) to a BCC + FCC dual-phase structure (x = 50), and then to a single FCC phase ($x \geq 60$). Figure 6b shows the enlarged XRD patterns in the 2θ range of 40–60° from Figure 6a. The characteristic diffraction peaks of the BCC phase remain nearly unchanged at first, followed by a gradual shift toward higher angles when $x > 20$. Similarly, the characteristic diffraction peaks of the FCC phase exhibit the same shifting trend when $x \geq 50$. The lattice parameters of each alloy calculated by Jade 6.5 software are summarized in Table 2. The lattice constant of the BCC phase decreases from 2.870 Å (x = 10) to 2.854 Å (x = 30) followed by a slight increase to 2.862 Å at x = 40. In contrast, the lattice constant of the FCC phase decreases continuously. Which may be mainly attributed to the substitution of larger Fe (1.26 Å) atoms by smaller Co (1.25 Å) and Ni (1.24 Å) atoms. The incorporation of Co and Ni atoms induces lattice contraction due to their smaller atomic radii. With x increased, the increasing atomic size mismatch among Fe, Co, and Ni further promotes lattice distortion.

Researchers claimed that valence electron concentration (*VEC*), mixing enthalpy (ΔH_{mix}), mixing entropy (ΔS_{mix}), atomic size difference (ΔR), electronegativity difference (ΔX), and solid-solution forming ability (Ω) affect the phase stability and microstructure of HEAs [49,50]. Accordingly, we calculated these parameters of the alloys, as listed in Table 3. It can be seen that ΔS_{mix} increase continuously with the increasing x, and only decreases slightly at x = 80. According to the criterion for MEAs, an alloy is classified as a MEA when $1.0R < \Delta S_{mix} < 1.5R$ (i.e., 8.314 $J \cdot mol^{-1} \cdot K^{-1} < \Delta S_{mix} < 12.471$ $J \cdot mol^{-1} \cdot K^{-1}$) [51]. Accordingly, the alloys with $x \leq 40$ in this work exhibit $\Delta S_{mix} < 8.314$ $J \cdot mol^{-1} \cdot K^{-1}$, fall into the low-entropy alloy (LEA) category, whereas those with $x \geq 50$ satisfy the criterion for MEAs. ΔH_{mix} remains negative for all compositions, decreasing to –1.5 at x = 50 and subsequently increasing. Meanwhile, ΔR, ΔX first rise and peaks at x = 50, respectively, then decreases. *VEC* increases continuously from 8.15 to 9.2. Ω first decreases to 9.683 at x = 30, followed by an upward trend. Guo et al. Claimed, $VEC < 6.87$ favors BCC phase formation, whereas $VEC > 8.0$ favors FCC formation [50]. Nevertheless, for $x \leq 40$, the alloys form a single BCC phase despite $VEC > 8.0$. This is attributed to the high Fe content (Fe being a strong BCC

stabilizer) by which the BCC phase is retained kinetically. At $x = 50$ ($VEC = 8.75$), the Fe is relatively reduced and an FCC phase begins to emerge. When $x \geq 60$, VEC continues to increase and the alloys own a single FCC phase. In addition, since $\Omega > 1.1$ and $\Delta H_{mix} < 0$, all the alloys possess a good solid-solution forming ability, meanwhile, the high-entropy effect effectively suppresses the precipitation of intermetallic compounds, favoring the formation of a single phase solid solution [49]. Both ΔR and ΔX reach their maxima at $x = 50$ ($\Delta R = 0.660\%$, $\Delta X = 3.419\%$), indicating that the atomic size mismatch is largest and the lattice distortion is severe at this composition.

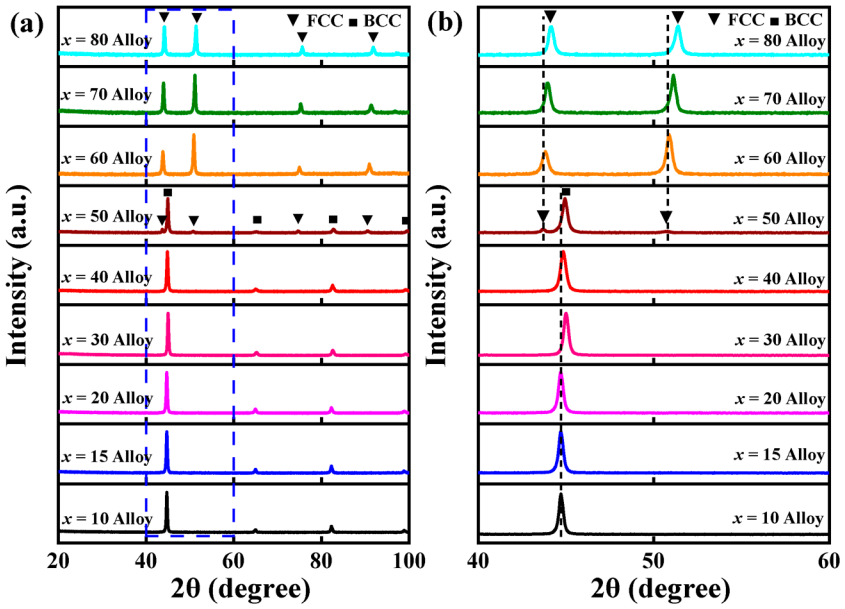


Figure 6. (**a**) XRD patterns of $Fe_{100-x}(Co_{0.5}Ni_{0.5})_x$ (x = 10–80 at%) alloys, (**b**) their enlarged views.

Table 2. Lattice constants of $Fe_{100-x}(Co_{0.5}Ni_{0.5})_x$ (x = 10–80 at%) alloys.

Alloys	Lattice Constants	
	BCC (Å)	FCC (Å)
$x = 10$	2.870 ± 0.001	-
$x = 15$	2.871 ± 0.001	-
$x = 20$	2.871 ± 0.001	-
$x = 30$	2.854 ± 0.003	-
$x = 40$	2.862 ± 0.001	-
$x = 50$	2.856 ± 0.002	3.599 ± 0.002
$x = 60$	-	3.591 ± 0.002
$x = 70$	-	3.575 ± 0.001
$x = 80$	-	3.561 ± 0.001

Table 3. The ΔS_{mix}, ΔH_{mix}, ΔR, ΔX, VEC, and Ω values of $Fe_{100-x}(Co_{0.5}Ni_{0.5})_x$ (x = 10–80 at%) alloys.

x	ΔS_{mix} (J·mol^{-1}·K^{-1})	ΔH_{mix} (kJ·mol^{-1})	ΔR (%)	ΔX (%)	VEC	Ω
10	3.279	−0.540	0.379	2.007	8.150	10.959
15	4.379	−0.765	0.452	2.393	2.225	10.312
20	5.313	−0.960	0.511	2.685	8.300	9.953
30	6.808	−1.260	0.592	3.090	8.450	9.683
40	7.901	−1.440	0.638	3.323	8.600	9.798
50	8.644	−1.500	0.660	3.419	8.750	10.255
60	9.053	−1.440	0.658	3.390	8.900	11.148

70	9.113	−1.260	0.645	3.232	9.050	12.779
80	8.771	−0.960	0.602	2.926	9.200	16.086

3.4. Microstructure

Figure 7 shows the SEM-BSE images and SEM-EDS maps of the $Fe_{100-x}(Co_{0.5}Ni_{0.5})_x$ (x = 10–80 at%) alloys. For the x = 15 and x = 40 alloys, Fe is enriched inside grains, while Ni is enriched at grain boundaries, Co is distributed homogeneously. To further quantitatively determine the elemental distribution, a line scan analysis was performed across a region traversing a grain boundary. Details are provided in Figure S1 of the Supplementary Materials. When x = 15, Co is uniformly distributed at a content of 7.5 ± 1.3 at%. Ni is enriched at the grain boundary, reaching 11.5 at%, while remaining uniformly distributed at 7.3 ± 1.5 at% within the grains. In contrast, Fe is depleted at the grain boundary with a content of 79.4 at%, compared to the value of 85.3 ± 2.9 at% within the grains. When x = 40, Co is likewise uniformly distributed at 20.0 ± 2.3 at%. Ni again exhibits grain-boundary segregation, 27.8 at% at the boundary versus a content of 19.6 ± 2.8 at% within the grains. Fe shows a corresponding depletion at the grain boundary 51.5% relative to the value of 60.3 ± 3.7 at% within the grains. However, no obvious elemental segregation or depletion is observed in the x = 50 and x = 70 alloys, where all elements are uniformly distributed. This indicates that the composition adjustment exert a remarkable influence on elemental distribution and phase constitution of the alloys. On the one hand, when $x \leq 40$, the alloys possess a single BCC phase, owing to Fe enrichment within grains, we propose that an Fe-Co phase with high magnetic moment may form in the alloys, which endows the BCC phase alloys with an extremely high M_s [52]. When $x \geq 50$, the alloy possess a BCC + FCC dual phase, the elemental segregation and Fe-Co phase disappear, so that the M_s decreases drastically. On the other hand, when $x \leq 40$, Ni tends to segregates at grain boundaries, generate a Ni-rich phase. This Ni-rich phase inhibits grain growth and strongly pins magnetic domain rotation, leading to a substantial increase in H_c [53]. When $x \geq 50$, the segregation and Ni-rich phase vanish, grain growth proceeds, and the domain-wall pinning effect is greatly weakened, which causes a decrease in H_c.

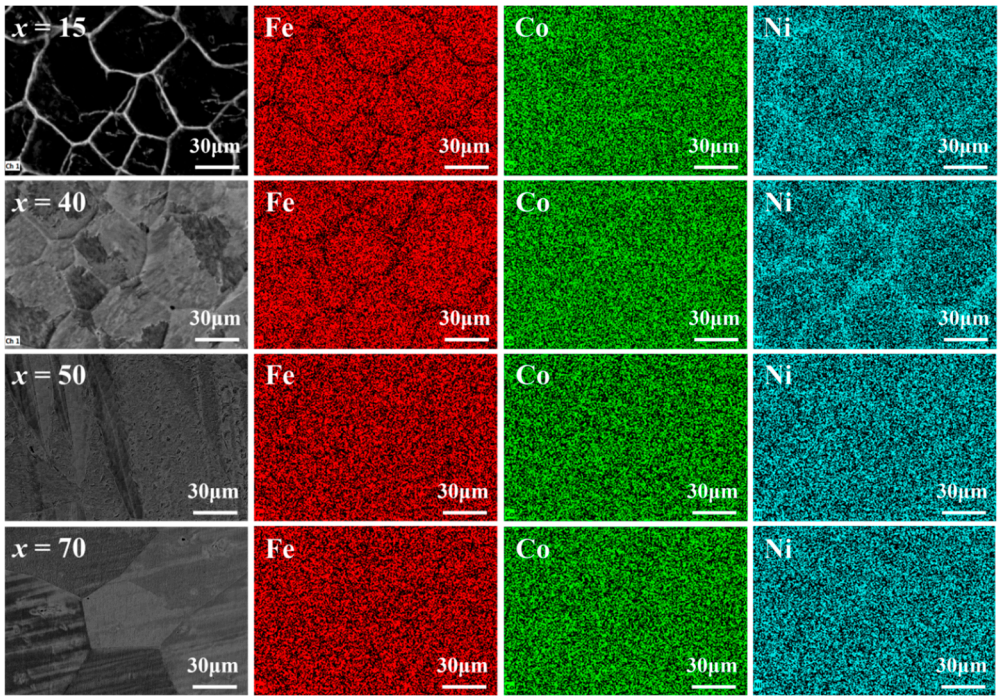


Figure 7. The SEM-BSE and SEM-EDS map images of the $Fe_{100-x}(Co_{0.5}Ni_{0.5})_x$ (x = 10–80 at%) alloys.

Figure 8 presents the phase constitution, grains, grain boundary characteristics, and strain concentration characteristics of the $Fe_{100-x}(Co_{0.5}Ni_{0.5})_x$ (x = 10–80 at%) alloys. Figure 8(a1–d1) reveal a gradual phase transition from BCC to FCC phase with increasing x. The x = 15 and 40 alloys exhibit a single BCC structure. When x = 50, a large fraction of the FCC phase emerges and coexists with the BCC phase, quantitative phase analysis reveals that the alloy consists of 58.3% BCC phase and 41.7% FCC phase. Further increasing to x = 70 results in a fully FCC structure. Figure 8(a2–d2) indicate significant grain coarsening with increasing x. When $x \leq 40$, the alloys exhibit relatively fine grain sizes, which undergo a slight refinement. Specifically, the average grain size decreases from 50 μm for the x = 15 alloy to 31 μm for the x = 40 alloy. It can be clearly observed that the grains in the x = 15 alloy are predominantly elongated, whereas those in the x = 40 alloy become more uniformly distributed with a nearly equiaxed grains. When $x \geq 50$, the grain size increases significantly, and is dominated by equiaxed grain. The x = 50 alloy contains several coarse elongated grains within the equiaxed grains, with an average grain size of 88 μm. In contrast, the x = 70 alloy exhibits a fully equiaxed grain with a substantially increased average grain size of 219 μm. The corresponding grain size distributions are shown in Figure 8(a3–d3). Figure 8(a4–d4) shows that the fraction of LAGBs markedly reduced with increasing x in the alloys. Grain boundaries with misorientation angles of 2–5° and 6–15°, representing LAGBs, are colored yellow and blue, respectively, whereas grain boundaries with misorientation angles greater than 15°, corresponding to HAGBs, are shown in purple. The grain boundaries in the x = 15 and 40 alloys are predominantly yellow and blue, indicating a high fraction of LAGBs. In contrast, the grain boundaries in the x = 50 and 70 alloys are mainly purple, demonstrating a significant reduction in the fraction of LAGBs and a corresponding predominance of HAGBs. The quantitative fractions of the different grain boundary types are summarized in Table 4. Figure 8(a5–d5) presents the kernel average misorientation (KAM) maps of the alloys, where blue represents regions with low strain, while green indicates pronounced strain concentration. With increasing x, the alloys exhibit a relatively high level of strain concentration at x = 15–40, and the strain shows a slight increase. However, the local strain decreases markedly for the x = 50 and 70 alloys. For the x = 50 alloy, strain concentration is mainly localized at the interfaces between the BCC and FCC phases. In contrast, almost no obvious strain concentration is observed in the x = 70 alloy. Overall, the increasing x results in a gradual transformation from a fine-grained BCC structure containing abundant LAGBs and severe local strain concentration to a coarse-grained single FCC structure characterized by predominant HAGBs and negligible strain concentration. To clarify the relationships between average grain size, LAGB fraction, KAM value, and H_c, we performed a quantitative analysis, as shown in Figure S2 of the Supplementary Materials. The variation trend of H_c is negatively correlated with the average grain size, whereas it is positively correlated with the LAGB fraction and KAM value.

Table 4. The LAGBs and HAGBs fractions of $Fe_{100-x}(Co_{0.5}Ni_{0.5})_x$ (x = 10–80 at%) alloys.

Alloys	LAGBs		HAGBs
	2–5° (%)	6–15° (%)	>15° (%)
x = 15	30	41.9	28.1
x = 40	33.5	47.6	18.9
x = 50	9.4	19.7	70.9
x = 70	0.4	12.0	87.6

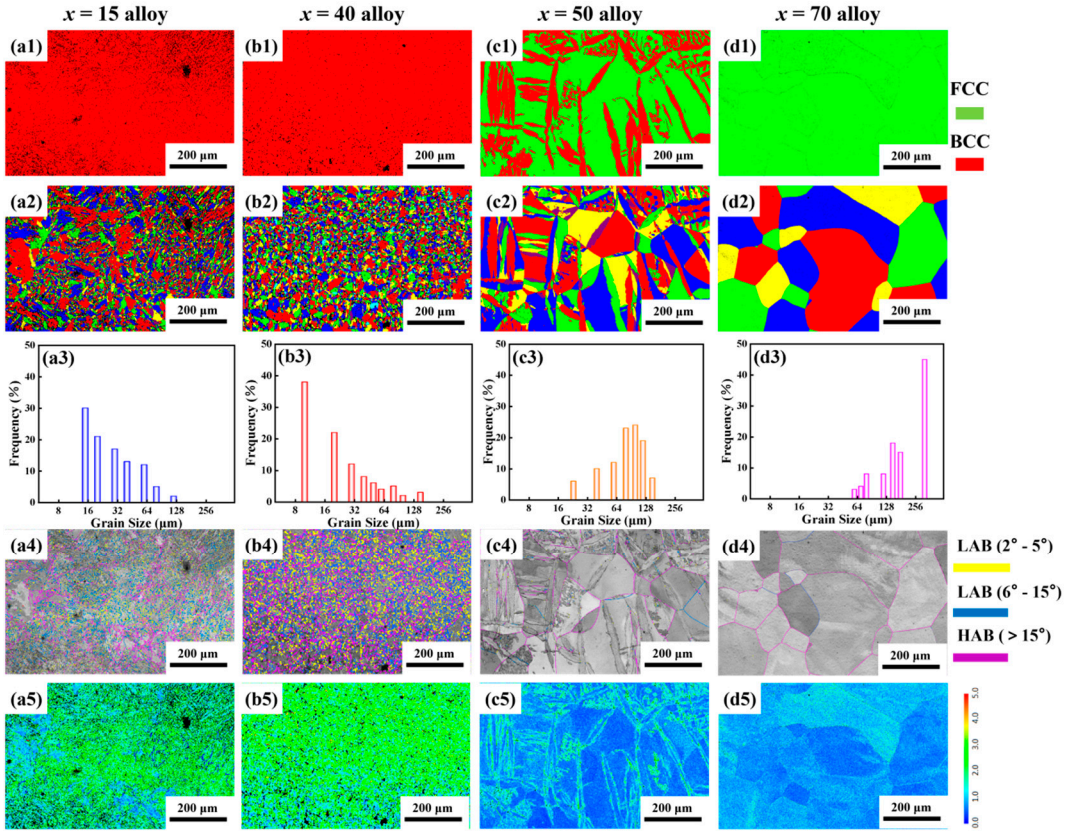


Figure 8. The EBSD images of the $Fe_{100-x}(Co_{0.5}Ni_{0.5})_x$ (x = 10–80 at%) alloys. (**a1–d1**) The phase maps, (**a2–d2**) The grain distribution maps, (**a3–d3**) The grain size distribution histogram, (**a4–d4**) The grain-boundary character distribution, (**a5–d5**) The kernel average misorientation (KAM) images.

4. Discussion

4.1. Mechanism of the Composition and Phase Constitution on M_s

It can be seen from the above results that the M_s of the $Fe_{100-x}(Co_{0.5}Ni_{0.5})_x$ (x = 10–80 at%) alloys decreases monotonically with the reduction of Fe content, dropping from 220 Am^2/kg to 138 Am^2/kg. It is mainly affected by composition and phase constitution.

Fe and Co are the dominant magnetic elements, the relative proportions of Fe and Co have a significant effect on the M_s of the alloy. As reported by Can et al. [54] in FeCo-based amorphous alloys, a decrease in Fe/Co ratio leads to a concurrent reduction in M_s. However, in this work, when $x \leq 40$, we consider that owing to the formation of the Fe–Co phase, the strong ferromagnetic exchange coupling between Fe and Co preserves an ultrahigh M_s (> 200 Am^2/kg) [52]. According to the Slater–Pauling rule, the average atomic magnetic moment of 3d transition metal alloys first increases and then decreases with rising *VEC*, and reaches the maximum value when Fe/Co ratio is 2.3:1 [52]. The calculated results in Table 3 confirm that the *VEC* of the alloys gradually increases. Since the Fe/Co is greater than 2.3:1 and lies before the highest magnetic moment point. Therefore, although the Fe content continuously decreases in the alloys, the enhanced magnetic moment of the Fe–Co phase originating from the rising *VEC* prevents a notable drop in M_s, which remains at an extremely high value.

When x = 50, M_s decreases sharply from 202 Am^2/kg to 169 Am^2/kg. We speculate that this originates from the disappearance of the BCC Fe–Co phase, this is supported by the homogeneous elemental distribution in the x = 50 alloy, see Figure 7. Furthermore, to verify that the M_s does not originate from the Fe–Co phase, we calculated the weighted M_s of the alloy at x = 50, which equals 162 Am^2/kg. This differs from the experimental results by

4%, which we consider to be within the error range and in good agreement with the measured data, confirming that the M_s of the alloy originates from the individual contributions of each constituent element. Moreover, the alloy possesses a BCC+FCC dual-phase structure, the lower M_s of the FCC phase further reduce the overall M_s of the alloy [45].

When $x \geq 60$, the alloys exhibit a single FCC phase, and M_s decreases continuously. This reduction is mainly attributed to the decrease in Fe content. Weighted M_s calculations reveal that M_s decreases by 10 Am^2/kg with every 10 at% reduction of Fe, which is consistent with the experimental results.

4.2. Mechanism of the Microstructure on H_c

The above results show that the H_c of the $Fe_{100-x}(Co_{0.5}Ni_{0.5})_x$ (x = 10–80 at%) alloys measured by either VSM or soft magnetic tester first increases gradually and then drops significantly as the Fe decreases. It reaches the maximum DC H_c of 1445 A/m at x = 40, while the minimum DC H_c of 36 A/m at x = 70. This non-monotonic variation is primarily attributed to microstructure evolution.

When $x \leq 40$, the DC H_c of the alloys increases from 289 A/m to 1445 A/m. It can be attributed to the following aspects: (1) Lattice distortion induces local lattice strain, which pins the magnetic domain walls when they pass through the distorted regions. Moreover, the lattice distortion intensifies progressively from x = 10 to x = 30. Even though it shows a slight recovery at x = 40, it still remains at a relatively high level, see Figure 6 and Table 2 [55]. (2) The segregation of Ni at grain boundaries induces compositional fluctuations and enhances magnetocrystalline anisotropy, forming strong pinning sites, and it is more pronounced at x = 40, see Figure 7 [53]. Both İçin and Özçelik et al. claimed that local chemical inhomogeneity weakens the exchange interactions within the Fe-Co-Ni sublattice, while simultaneously acting as effective pinning centers for domain-wall motion and thereby increasing the H_c [56,57]. (3) Fine grain size increases the number of grain boundaries, which strongly pin magnetic domain walls [21]. Moreover, LAGBs among grain boundaries exert a stronger pinning effect on magnetic domain walls [43]. In addition, abundant grain boundaries together with lattice distortion induce remarkable strain concentration, further hindering the motion of magnetic domain walls, see Figure 8 [40,58]. All these factors are continuously enhanced with the reduction of Fe. Collectively, they impose the strongest restriction on magnetic domain wall motion for the x = 40 alloy, which therefore possesses the maximum H_c.

When x = 50, the DC H_c of the alloys decreases sharply from 1445 A/m to 281 A/m. It can also be attributed to the following aspects: (1) Lattice distortion still remains. (2) The insignificant segregation of Ni at grain boundaries greatly reduces the pinning effect on magnetic domain walls. This is because the alloy owns a BCC + FCC dual-phase, and the FCC structure possesses a high solid solubility for Ni. Thus, Ni can dissolve uniformly into the lattice without segregation at grain boundaries, see Figure 7. (3) The grains grow obviously, the number of grain boundaries decreases drastically, and phase boundaries form instead. Meanwhile, the fraction of LAGBs is also greatly reduced. Although lattice distortion still exists, strain is mainly concentrated at phase boundaries, which is markedly lower than x = 40, see Figure 8. Although lattice distortion still hinders magnetic domain motion, grain growth, a substantial reduction in the number of LAGBs, and marked reduction of strain concentration collectively reduce the resistance to domain-wall motion to a greater extent. This combined effect leads to a rapid decrease in H_c of the x = 50 alloy.

When $x \geq 60$, the DC H_c of the alloys decreases further from 281 A/m to 36 A/m. This is also caused by three factors: (1) The lattice constant of the alloy decreases continuously, indicating gradual attenuation of lattice distortion, which weakens the pinning effect on magnetic domain walls, see Table 2. (2) Ni does not segregate at grain boundaries, so there is no domain-wall pinning originating from segregation. (3) The alloy possesses a single

FCC phase with larger grain size and a further reduced number of grain boundaries, which further weakens the pinning effect on domain walls. Moreover, the phase boundaries disappear, and the domain-wall hindrance originating from incoherent two phases vanishes. In addition, the quantity of LAGBs decreases to a negligible level, and strain concentration barely exists inside the alloy, see Figure 8. Consequently, the domain-wall blocking effect caused by LAGBs and strain concentration is greatly weakened. The combined effect of the above factors yields the minimum H_c of 36 A/m for the x = 70 alloy.

According to Figure S2 (Supplementary Material), the variation trend of H_c is negatively correlated with the average grain size, whereas it is positively correlated with the LAGB fraction and KAM value. This trend confirms that the H_c evolution may jointly governed by grain size, LAGB fraction, and local strain concentration. Finer grains and a higher LAGB fraction introduce more effective pinning sites, while elevated KAM indicates stronger local strain fields that further impede domain-wall motion. Combined with the EDS line-scan results (Figure S1), which confirm Ni segregation at grain boundaries in the BCC alloys. These quantitative correlations provide direct and self-consistent evidence for the proposed domain-wall pinning mechanism underlying the non-monotonic H_c variation.

5. Conclusions

In this work, a series of $Fe_{100-x}(Co_{0.5}Ni_{0.5})_x$ (x = 10–80 at%) alloys were fabricated by vacuum arc melting. The combined influences of compositional adjustment on phase constitution, microstructure, mechanical hardness and soft-magnetic properties were systematically investigated, and the underlying structure-property mechanisms were revealed. The main conclusions are summarized as follows:

1. As the x increases, the alloy undergoes a phase evolution from single BCC phase ($x \leq 40$), to BCC+FCC dual-phase structure (x = 50), and finally to single FCC phase ($x \geq 60$). Lattice parameters of both BCC and FCC phases gradually decrease due to atomic substitution of Fe by smaller-sized Co and Ni atoms. Vickers hardness reaches maximum 287 HV at x = 40 for single-BCC alloys, and drops sharply after FCC phase appears.
2. M_s monotonically decreases from 220 Am^2/kg to 138 Am^2/kg with increasing x. All BCC-type alloys with $x \leq 40$ possess high M_s values exceeding 200 Am^2/kg, and such ultra-high M_s originates from Fe-Co-rich BCC phase. After the emergence of FCC phase at x = 50, M_s declines significantly, which can be well explained by weighted superposition of elemental magnetic contributions.
3. H_c exhibits a non-monotonic trend: it rises to maximum value at x = 40 and then decreases. For BCC-phase alloys ($x \leq 40$), Ni segregation at grain boundaries, fine grains, high fraction of LAGBs and severe local strain concentration collectively produce strong pinning effects on magnetic domain walls, leading to high H_c. At x = 50, Ni segregation disappears upon forming FCC phase; grain coarsening, reduction of LAGBs and relieved strain concentration weaken domain-wall pinning and sharply reduce H_c. The single-FCC alloy at x = 70 delivers the best DC soft-magnetic performance: H_c = 36 A/m, μ_i of 539 and μ_m of 1464.
4. Without introducing additional alloying elements, tuning intrinsic Fe-Co-Ni atomic ratio is an effective strategy to tailor microstructure and soft-magnetic performance of ternary MEAs. This study provides fundamental understanding and practical composition guidance for developing high-performance soft-magnetic MEAs.

https://doi.org/10.3390/e28121313

Supplementary Materials: The following supporting information can be downloaded at: https://www.mdpi.com/article/10.3390/e28121313/s1, Table S1: The Vickers hardness of $Fe_{100-x}(Co_{0.5}Ni_{0.5})_x$ (x = 10–80 at%) alloys. Figure S1: Line scan regions and elemental distribution profiles along the scan line in the x = 15 and x = 40 alloys. Figure S2. Quantitative relationships between average grain size, LAGB fractions, KAM values and H_c.

Author Contributions: Investigation, methodology, formal analysis, writing—original draft preparation, P.J.; data curation, visualization, Z.H.; data curation, visualization, N.L.; data curation, validation, S.Z.; writing—review and editing, H.X.; supervision, project administration, H.X. and X.T. All authors have read and agreed to the published version of the manuscript.

Funding: This work was supported by the National Natural Science Foundation of China (grant numbers 51971125 and 52401202).

Institutional Review Board Statement: Not applicable.

Data Availability Statement: The data presented in this study are available on request from the corresponding author.

Conflicts of Interest: Author Shuyan Zhang was employed by the Suzhou Wave Vector Advanced Materials Technology Co., Ltd. The remaining authors declare that the research was conducted in the absence of any commercial or financial relationships that could be construed as a potential conflict of interest.

References

1. Silveyra, J.M.; Ferrara, E.; Huber, D.L.; Monson, T.C. Soft magnetic materials for a sustainable and electrified world. *Science* **2018**, *362*, eaao0195. https://doi.org/10.1126/science.aao0195.
2. Ouyang, G.F.; Chen, X.; Liang, Y.F.; Macziewski, C.; Cui, J. Review of Fe-6.5 wt% Si high silicon steel-A promising soft magnetic material for sub-kHz application. *J. Magn. Magn. Mater.* **2019**, *481*, 234–250. https://doi.org/10.1016/j.jmmm.2019.02.089.
3. Li, X.S.; Zhou, J.; Shen, L.Q.; Sun, B.A.; Bai, H.Y.; Wang, W.H. Exceptionally high saturation magnetic flux density and ultralow coercivity via an amorphous–nanocrystalline transitional microstructure in an FeCo-based alloy. *Adv. Mater.* **2023**, *35*, 2205863. https://doi.org/10.1002/adma.202205863.
4. Ma, M.Y.; Zhao, X.; Sun, X.Y.; Jiang, J.T.; Shao, W.Z.; Zhen, L. Microstructure evolution and strengthening mechanism of FeCo-1.5V0.5Nb0.4W soft magnetic alloy rolled strip with high yield strength and low coercivity. *Acta Mater.* **2024**, *268*, 119793. https://doi.org/10.1016/j.actamat.2024.119793.
5. Yang, S.Y.; Zang, B.W.; Xiang, M.L.; Shen, F.Y.U.; Song, L.J.; Gao, M.; Zhang, Y.; Huo, J.T.; Wang, J.Q. Designing Fe-based amorphous alloys with both ultra-high magnetization and ultra-low coercivity through artificial intelligence. *Adv. Funct. Mater.* **2025**, *35*, 2425588. https://doi.org/10.1002/adfm.202425588.
6. Lu, S.H.; Wang, M.G.; Zhao, Z.K. Recent advances and future developments in Fe-based amorphous soft magnetic composites. *J. Non-Cryst. Solids.* **2023**, *616*, 122440. https://doi.org/10.1016/j.jnoncrysol.2023.122440.
7. Sun, J.J.; Ren, J.Y.; Li, J.; Huang, Y.J. Measurement and analysis of magnetic properties of permalloy for magnetic shielding devices under different temperature environments. *Materials* **2023**, *16*, 3253. https://doi.org/10.3390/ma16083253.
8. Popa, F.; Isnard, O.; Neamțu, B.V.; Chicinaș, I. Frequency properties of polymer bonded compacts obtained from ball milled permalloy powders with Mo and Cu additions. *Materials* **2023**, *16*, 592. https://doi.org/10.3390/ma16020592.
9. Chen, C.; Cao, Z.F.; Cui, L.; Chang, F.Y.; Xiao, Y.; Wu, L.N.; Ge, X.Y. Tailoring magnetic properties and power loss in low-temperature sintered NiCuZn ferrites with BMLS-CaTiO3/BaTiO3 composite additives. *Materials* **2025**, *18*, 5202. https://doi.org/10.3390/ma18225202.
10. Shaikh, B.B.R.; Toksha, B.G.; Shirsath, S.E.; Chatterjee, A.; Tonde, S.; Chishty, S.Q. Microstructure, magnetic, and dielectric interplay in NiCuZn ferrite with rare earth doping for magneto-dielectric applications. *J. Magn. Magn. Mater.* **2021**, *537*, 168229. https://doi.org/10.1016/j.jmmm.2021.168229.

11. Ma, D.J.; Tian, B.Z.; Zheng, X.; Li, Y.L.; Xu, S.B.; Pei, R.L. Study of high-silicon steel as interior rotor for high-speed motor considering the influence of multi-physical field coupling and slotting process. *Materials* **2022**, *15*, 8502. https://doi.org/10.3390/ma15238502.
12. Cantor, B.; Chang, I.T.H.; Knight, P.; Vincent, A.J.B. Microstructural development in equiatomic multicomponent alloys. *Mater. Sci. Eng. A* 2004, 375–377, 213–218. https://doi.org/10.1016/j.msea.2003.10.257.
13. Yeh, J.W.; Chen, S.K.; Lin, S.J.; Gan, J.Y.; Chin, T.S.; Shun, T.T.; Tsau, C.H.; Chang, S.Y. Nanostructured High-Entropy Alloys with Multiple Principal Elements: Novel Alloy Design Concepts and Outcomes. *Adv. Eng. Mater.* **2004**, *6*, 299–303. https://doi.org/10.1002/adem.200300567.
14. Yeh, J.W. Alloy design strategies and future trends in high-entropy alloys. *JOM* **2013**, *65*, 1759–1771. https://doi.org/10.1007/s11837-013-0761-6.
15. Onawale, O.T.; Cobbinah, P.V.; Nzeukou, R.A.; Matizamhuka, W.R. Synthesis route, microstructural evolution, and mechanical property relationship of high-entropy alloys (HEAs): A review. *Materials* **2021**, *14*, 3065. https://doi.org/10.3390/ma14113065.
16. Balaji, V.; Anthony Xavior, M. Development of high entropy alloys (HEAs): Current trends. *Heliyon* **2024**, *10*, e26464. https://doi.org/10.1016/j.heliyon.2024.e26464.
17. Garcia Filho, F.D.C.; Ritchie, R.O.; Meyers, M.A.; Monteiro, S.N. Cantor-derived medium-entropy alloys: Bridging the gap between traditional metallic and high-entropy alloys. *J. Mater. Res. Technol*. **2022**, *17*, 1868–1895. https://doi.org/10.1016/j.jmrt.2022.01.118.
18. Nutor, R.K.; Cao, Q.P.; Wang, X.D.; Ding, S.Q.; Zhang, D.X.; Jiang, J.Z. Accelerated emergence of CoNi-based medium-entropy alloys with emphasis on their mechanical properties. *Curr. Opin. Solid State Mater. Sci*. **2022**, *26*, 101032. https://doi.org/10.1016/j.cossms.2022.101032.
19. Ge, P.H.; Zhang, Y.; Li, Z. Soft-magnetic and mechanical behaviors of heterostructured FeCoNi medium-entropy alloys. *Acta Metall. Sin*. **2025**, *61*, 1119–1128. https://doi.org/10.11900/0412.1961.2023.00215.
20. Hu, X.Z.; Jia, X.Q.; Xu, Z.L.; Chen, X.L.; Zhang, D.B.; Xia, A.L. Forming process, microstructure and magnetic properties of FeCoNi medium-entropy alloy fabricated via selective laser melting: Insights into the building direction-dependent anisotropy. *J. Alloys Compd.* **2026**, *1077*, 189516. https://doi.org/10.1016/j.jallcom.2026.189516.
21. Cao, Z.R.; Zhang, P.C.; An, B.L.; Li, D.W.; Yu, Y.; Pan, J.; Zhang, C.; Liu, L. In situ phase engineering during additive manufacturing enables high-performance soft-magnetic medium-entropy alloys. *Nat. Commun*. **2024**, *15*, 9747. https://doi.org/10.1038/s41467-024-54133-0.
22. Li, X.H.; Li, W.B.; Wang, R.; Ping, E.S.; Yang, S.F. Effect of different AlSi content on microstructure and magnetic properties of FeCoNi(AlSi)x HEA. *Arch. Metall. Mater.* **2025**, *70*, 1507–1513. Available online: https://www.imim.pl/files/archiwum/Vol4_2025/03.pdf (accessed on 22 November 2026).
23. Zhang, B.; Duan, Y.P.; Cui, Y.L.; Ma, G.J.; Wang, T.M.; Dong, X.L. A new mechanism for improving electromagnetic properties based on tunable crystallographic structures of FeCoNiSixAl0.4 high entropy alloy powders. *RSC Adv.* **2018**, *8*, 14936–14946. https://doi.org/10.1039/c8ra01762j.
24. Peng, W.F.; Xia, Y.B.; Xu, H.; Tan, X.H. Tuning corrosion resistance and AC soft magnetic properties of Fe-Co-Ni-Al medium-entropy alloy via Ni content. *Entropy* **2024**, *26*, 1038. https://doi.org/10.3390/e26121038.
25. Tan, L.P.; Chaudhary, V.; Tsakadze, Z.; Ramanujan, R.V. Rapid multiple property determination from bulk materials libraries prepared from chemically synthesized powders. *Sci. Rep*. **2022**, *12*, 9504. https://doi.org/10.1038/s41598-022-13691-3.
26. Huang, Y.L.; Qian, C.H.; Bian, R.Y.; Zhu, X.Q.; Jin, Y.R. Synergistic enhancement of mechanical and magnetic properties in a FeCoNi medium-entropy alloy by ultra-severe plastic deformation. *J. Alloys Compd*. **2026**, *1055*, 186402. https://doi.org/10.1016/j.jallcom.2026.186402.
27. Cardoso, F.M.; Froes, F.; Bormio-Nunes, C. A novel high entropy FeCoNi(GaCu)1.0 alloy with attractive soft magnetic properties. Physica B Condens. *Matter* **2024**, *695*, 416495. https://doi.org/10.1016/j.physb.2024.416495.
28. Akbari, A.; Vafaei, R.; Jamali, H.; Mohammad Sharifi, E. Effects of annealing and cold rolling on microstructural features, magnetic properties, tensile behavior and electrical resistance of FeCoNi(MnAl)x high entropy alloys. *Intermetallics* **2024**, *175*, 108521. https://doi.org/10.1016/j.intermet.2024.108521.
29. Javdan, M.; Gheisari, K.; Reihanian, M. Mechanically alloyed (FeCoNi)75Cu25−xSix high entropy alloys: Phase evaluation and magnetic properties. *J. Alloys Compd*. **2023**, *952*, 170030. https://doi.org/10.1016/j.jallcom.2023.170030.

30. Chen, T.; Chen, W.P.; Jiang, Z.F.; Zhu, D.Z.; Fu, Z.Q. An in-situ formed TiC/FeCoNi medium-entropy composite with excellent combination of mechanical and soft magnetic properties. *Vacuum* **2023**, *218*, 112601. https://doi.org/10.1016/j.vacuum.2023.112601.
31. Zuo, T.T.; Li, R.B.; Ren, X.J.; Zhang, Y. Effects of Al and Si addition on the structure and properties of CoFeNi equal atomic ratio alloy. *J. Magn. Magn. Mater*. **2014**, *371*, 60–68. https://doi.org/10.1016/j.jmmm.2014.07.023.
32. Zheng, D.; Xu, X.S.; Wei, D.X.; Zheng, G.; Qi, Z.X.; Chen, Y.; Chen, G. Mechanical and magnetic properties of soft magnetic high-entropy alloys based on nano-precipitation regulation. *Mater. Sci. Eng. A* **2026**, *972*, 150561. https://doi.org/10.1016/j.msea.2026.150561.
33. Mohapatra, S.K.; Kumari, P.; Rastogi, S.; Singh, S.; Shahi, R.R. Face centred cubic Co35Fe10Mn5Ni30Ti20 high entropy alloy with enhanced soft magnetic and corrosion properties. *J. Magn. Magn. Mater.* **2025**, *630*, 173392. https://doi.org/10.1016/j.jmmm.2025.173392.
34. Mohapatra, S.K.; Kumari, P.; Choudhary, R.J.; Lakhani, A.; Shahi, R.R. Excellent soft magnetic with high electrical and corrosion resistance properties of Co35Cu5Fe10Ni30Ti20 high entropy alloy. *J. Alloys Compd*. **2025**, *1027*, 180584. https://doi.org/10.1016/j.jallcom.2025.180584.
35. Dong, P.L.; Huang, L.F.; Yang, Q.J.; Zhao, X.J.; Zhong, Z.Y.; Li, J.F. Mechanical and magnetic properties of nonequiatomic Fe33Co28Ni28Ta5Al6 high entropy alloy by laser melting deposition. *Vacuum* **2024**, *220*, 112854. https://doi.org/10.1016/j.vacuum.2023.112854.
36. Zuo, T.T.; Zhang, M.; Liaw, P.K.; Zhang, Y. Novel high entropy alloys of FexCo1-xNiMnGa with excellent soft magnetic properties. *Intermetallics* **2018**, *100*, 1–8. https://doi.org/10.1016/j.intermet.2018.05.014.
37. Liang, Y.X.; Mao, Z.X.; Wu, Y.C.; Wang, H.Y.; Chen, Y.X.; Tan, X.H.; Xu, H. Cr-induced microstructural changes to synergistically enhance the soft magnetic properties and corrosion resistance of FeCoNiCrx medium-entropy alloys. *J. Alloys Compd.* **2026**, *1066*, 188235. https://doi.org/10.1016/j.jallcom.2026.188235.
38. Tan, X.H.; Li, J.Y.; Zhang, S.Q.; Xu, H. The Si-doped BCC-based high-entropy alloy to overcome soft magnetic–mechanical properties trade-off via coherent B2 nanoprecipitates. *Mater. Charact*. **2024**, *217*, 114402. https://doi.org/10.1016/j.matchar.2024.114402.
39. Zhang, H.L.; Lei, S.; Li, Y.; Cui, S.J.; Hu, S.S.; Wang, P. Microstructural evolution and magnetic and corrosion properties of FeCoNiAl0.2Yx high-entropy alloys. *ECS J. Solid State Sci. Technol.* **2023**, *12*, 113009. https://doi.org/10.1149/2162-8777/ad0876.
40. Tan, X.H.; Tang, Y.J.; Tan, Y.F.; Deng, Q.; Jiao, H.S.; Yang, Y.; Xu, H. Correlation between microstructure and soft magnetic parameters of Fe-Co-Ni-Al medium-entropy alloys with FCC phase and BCC phase. *Intermetallics* **2020**, *126*, 106898. https://doi.org/10.1016/j.intermet.2020.106898.
41. Li, Z.; Xu, H.; Gu, Y.; Pan, M.X.; Yu, L.Y.; Tan, X.H.; Hou, X.L. Correlation between the magnetic properties and phase constitution of FeCoNi(CuAl)0.8Gax ($0 \le x \le 0.08$) high-entropy alloys. *J. Alloys Compd*. **2018**, *746*, 285–291. https://doi.org/10.1016/j.jallcom.2018.02.189.
42. Wu, Z.Y.; Li, B.; Chen, M.Y.; Yang, Y.; Zheng, R.Y.; Yuan, L.; Li, Z.; Tan, X.H.; Xu, H. Tailoring magnetic property and corrosion resistance of FeCoNiCuAl high-entropy alloy with Ce additive. *J. Alloys Compd*. **2022**, *901*, 163665. https://doi.org/10.1016/j.jallcom.2022.163665.
43. Tan, X.H.; Li, J.Y.; Zhang, S.Q.; Xu, H. Enhanced DC and AC soft magnetic properties of Fe-Co-Ni-Al-Si high-entropy alloys via texture and iron segregation. *Metals* **2024**, *14*, 1113. https://doi.org/10.3390/met14101113.
44. Li, Z.; Zhang, Z.H.; Liu, X.L.; Li, H.X.; Zhang, E.P.; Bai, G.H.; Xu, H.; Liu, X.G.; Zhang, X.F. Strength, plasticity and coercivity tradeoff in soft magnetic high-entropy alloys by multiple coherent interfaces. *Acta Mater*. **2023**, *254*, 118970. https://doi.org/10.1016/j.actamat.2023.118970.
45. Tan, X.H.; Chen, L.M.; Lv, M.X.; Peng, W.F.; Xu, H. Tailoring mechanical and magnetic properties in dual-phase FeCoNi(CuAl)0.8 high-entropy alloy. *Materials* **2023**, *16*, 7222. https://doi.org/10.3390/ma16227222.
46. Günen, A.; Keddam, M.; Sunbul, S.E.; Icin, K.; Doleker, K.M.; Gok, M.S.; Dal, S.; Erdogan, A. Powder-pack boronizing of CoCrFeNiAl0.5Nb0.5 HEA: Modeling of kinetics, microstructural, mechanical, and tribological characterizations. *J. Alloys Compd.* **2022**, *929*, 167310. https://doi.org/10.1016/j.jallcom.2022.167310.
47. Atam, D.; Sunbul, S.E.; Icin, K.; Döleker, K.M.; Gök, M.S.; Erdoğan, A. Boriding effect on CrFeMnNbNi high entropy alloy: Microstructure, micro-nano properties, wear behaviour. *Tribol. Int*. **2025**, *203*, 110410. https://doi.org/10.1016/j.triboint.2024.110410.

48. Çaliş, İ.; Günen, A.; Sünbül, S.E.; İçin, K.; Döleker, K.M.; Gök, M.S.; Erdoğan, A. Effect of boriding process temperature on microstructure, mechanical properties, and wear behavior of Al0.25CoCr1.5FeMo0.5Ni HEA. *Metals Mater. Int.* 2026. https://doi.org/10.1007/s12540-026-02227-3.
49. Yang, X.; Zhang, Y. Prediction of high-entropy stabilized solid-solution in multi-component alloys. *Mater. Chem. Phys.* **2012**, *132*, 233–238. https://doi.org/10.1016/j.matchemphys.2011.11.021.
50. Guo, S.; Ng, C.; Lu, J.; Liu, C.T. Effect of valence electron concentration on stability of fcc or bcc phase in high entropy alloys. *J. Appl. Phys.* **2011**, *109*, 103505, https://doi.org/10.1063/1.3587228.
51. Cheng, C.Y.; Yang, Y.C.; Zhong, Y.Z.; Chen, Y.Y.; Hsu, T.; Yeh, J.W. Physical metallurgy of concentrated solid solutions from low-entropy to high-entropy alloys. *Curr. Opin. Solid State Mater. Sci.* **2017**, *21*, 299–311. https://doi.org/10.1016/j.cossms.2017.09.002.
52. Hasegawa, T.; Niibori, T.; Takemasa, Y.; Oikawa, M. Stabilisation of tetragonal FeCo structure with high magnetic anisotropy by the addition of V and N elements. *Sci. Rep*. **2019**, *9*, 5248. https://doi.org/10.1038/s41598-019-41825-7.
53. Lan, X.J.; Wang, J.Y.F.; Liu, L.G.; Xu, Y.L.; Yang, C.J.; Zhang, M. From solid-solution strengthening to grain boundary segregation: A study on the mechanism of magnetic property evolution in Ni-doped Fe-5.5Si soft magnetic composites. *Micromachines* **2026**, *17*, 852. https://doi.org/10.3390/mi17070852.
54. Can, H.; Icin, K.; Akyol, S.; Topal, U.; Öztürk, S.; Sozeri, H. The magnetic field sensing performance of FeCo -based soft magnetic alloys with varying Fe/Co ratio. *J. Alloys Compd.* **2023**, *966*, 171515. https://doi.org/10.1016/j.jallcom.2023.171515.
55. Zhang, H.; Yang, Y.X.; Liu, L.; Chen, C.; Wang, T.; Wei, R.; Zhang, T.; Dong, Y.Q.; Li, F.S. A novel FeCoNiCr0.2Si0.2 high entropy alloy with an excellent balance of mechanical and soft magnetic properties. *J. Magn. Magn. Mater.* **2019**, *478*, 116–121. https://doi.org/10.1016/j.jmmm.2019.01.096.
56. İçin, K. Investigation of phase transformation related magnetic properties of Ti addition to FeCoCuNiMn and FeCoCuNiAl high entropy alloys by vacuum arc melting, Mater. *Today Commun*. **2024**, *39*, 108821. https://doi.org/10.1016/j.mtcomm.2024.108821.
57. Özçelik, İ.C.; Sünbül, S.E.; Bilgin, S.; Öztürk, S.; İçin, K. Role of Al/Si ratio on phase evolution, magnetic properties, and hardness of Fe-Co-Ni-Al-Si non-equiatomic high-entropy Alloys. *Solid State Sci*. **2026**, *181*, 108465. https://doi.org/10.1016/j.solidstatesciences.2026.108465.
58. Deng, Q.; Tang, Y.J.; Tan, Y.F.; Tan, X.H.; Yang, Y.; Xu, H. Effect of grain boundary character distribution on soft magnetic property of face-centered cubic FeCoNiAl0.2 medium-entropy alloy. *Mater. Charact.* **2020**, *159*, 110028. https://doi.org/10.1016/j.matchar.2019.110028.

Disclaimer/Publisher's Note: The statements, opinions and data contained in all publications are solely those of the individual author(s) and contributor(s) and not of MDPI and/or the editor(s). MDPI and/or the editor(s) disclaim responsibility for any injury to people or property resulting from any ideas, methods, instructions or products referred to in the content.